Geophys. J. Int. (2003) **154,** 515–532

Radar Doppler velocimetry of volcanic eruptions: theoretical considerations and quantitative documentation of changes in eruptive behaviour at Stromboli volcano, Italy

M. Hort,* R. Seyfried and M. Vöge*

Abteilung für Vulkanologie und Petrologie, GEOMAR Forschungszentrum, Kiel, Germany. E-mail: hort@dkrz.de

Accepted 2003 March 5. Received 2003 February 12; in original form 2002 July 24

SUMMARY

The use of radar Doppler velocimetry for the observation of volcanic activity is new. We used this method to continuously observe the activity of one vent of Stromboli volcano, Italy, from the end of 2000 April until early May. During this period we recorded 702 eruptions, 132 of which occurred before a strong rain storm passed over the island on April 29. In order to interpret the recorded Doppler data we developed a program that simulates different strombolian eruption scenarios, for which we then calculate the theoretical Doppler spectra. Comparing our theoretical data with the observed data we are able to show that most of the eruptions are nearly vertical, although we did observe only one component of the eruption vector with our Doppler radar. One of the most interesting features of the data set is a significant change in eruptive behaviour that correlates with the occurrence of the rain storm: we find that on average the eruption duration increased by a factor of 2, eruptive velocities were much higher and indirect evidence indicates that the average particle diameter of the erupted material decreased. This change may have several causes, but the coincidence with the rain storm may be evidence of magma–water interaction and feedback on the volcanic activity. If the fluid source (rain) changing the eruptive style is at the surface and in near-surface layers then the main control on final eruption dynamics at Stromboli volcano must also be in rather shallow regions.

Key words: Doppler radar, Stromboli, volcanic activity.

1 INTRODUCTION

Understanding the dynamics of explosive volcanic eruptions is still a major challenge in volcanology. Besides several theoretical studies (e.g. Wilson & Head 1981; Woods 1995; Proussevitch & Sahagian 1998; Herzog *et al.* 1998; Papale 1999) and experimental investigations (e.g. Jaupart & Vergniolle 1988; Mader *et al.* 1997; Seyfried & Freundt 2000), various attempts have been made to unravel the mystery of explosive volcanic eruptions through detailed geophysical measurements (e.g. Chouet *et al.* 1999; Ripepe & Gordeev 1999; Neuberg 2000; Aster *et al.* 2000, and others papers in that *J. Volc. Geotherm. Res.* special issue). Most of those field measurements were carried out with short-period seismometers as well as broadband seismic stations. In recent years many seismological observations have been complemented by infrasonic measurements using pressure sensors (Ripepe 1996) or very sensitive microphones (Vergniolle & Brandeis 1994).

So far very few studies (Chouet *et al.* 1974; Blackburn *et al.* 1976; Head & Wilson 1987; Weill *et al.* 1992; Ripepe *et al.* 1993; Hort & Seyfried 1998; Dubosclard *et al.* 1999) have attempted to characterize the dynamics of volcanic eruptions through *in situ* measurements of volcanic eruption velocities. The main drawback of those aforementioned experiments is that only one (sodar and radar technique) or two (photographic methods) components of the eruption vector are recorded at one time and in order to recover the complete eruption vector assumptions have to be made. Up to now the only 3-D measurement of volcanic eruption velocities has been carried out at Stromboli volcano, Italy, by Hort *et al.* (2001), where they found that the eruption vector rotated slightly during the eruption. Each of the different methods has its advantage and disadvantages. Whereas photographic methods give 2-D images of the eruption scene, the minimum size of a particle that can be resolved is usually limited. For example, Ripepe *et al.* (1993) were able to resolve particles as small as 10 cm, and Chouet *et al.* (1974) resolved particles down to 2.5 mm. Most of the observations in the case of photographic methods are carried out during the night because of the much better visibility of incandescent particles. This makes photographic methods somewhat unsuitable for a continuous monitoring task. However, in the future new image processing tools and infrared sensitive detectors should be able to overcome some of these disadvantages (e.g. Dehn *et al.* 2001).

*Now at: Institut für Geophysik, Universität Hamburg, Hamburg, Germany.

Nevertheless, interesting results have been achieved using photographic methods. Using an infrared sensitive film, Ripepe *et al.* (1993) were able to identify three different eruption types at Stromboli. Type 1 was characterized by a single explosive event, type 2 by two explosions following each other instantaneously (the first two types were observed at the southwestern crater) and a third type (observed at the northeastern crater) characterized by a temporal increase of the amount of erupted material. Each eruption lasted for 10–15 s. The other important aspect of this study was a correlation between the mass eruption rate and seismological data. This indicated an inverse proportionality between the explosive dynamics and the radiated seismic energy. Chouet *et al.* (1974) focused on eruption velocities and tried to determine the speed of gas and particles separately. They found that the gas velocities were significantly larger than the particle velocities and that the eruptive velocities for relatively large eruptions was between 2.6 and 72 m s^{-1} with an average particle size of 2.2 cm.

The advantage of Doppler methods compared with photographic methods is that the detectable particle size depends only on the transmitted frequency and continuous observations, including on-line processing of the data, is rather straightforward. The main problem with Doppler sodar measurements is that assumptions concerning the speed of sound in the eruption column have to be made (Weill *et al.* 1992) in order to calculate the eruption velocity. This problem does not arise when using radar. Radar can be used either as a plused (Dubosclard *et al.* 1999) or as a continuous wave (Hort & Seyfried 1998) system. The main advantage of a continuous wave system is its low power consumption. However, the temporal resolution is not as good as with a pulsed system. Both systems have been used in test studies for the observation of volcanic eruption velocities, the pulsed system at Mt Etna (Dubosclard *et al.* 1999) and the continuous wave system at Stromboli volcano (Hort & Seyfried 1998; Seyfried & Hort 1999).

In this paper we report results of the first continuous observation of volcanic eruption velocities at Stromboli volcano. The goals of the study were to first test our much improved radar system and to characterize the eruption dynamics of one of the vents at Stromboli volcano. In the following we first describe our experiment at Stromboli, including a detailed discussion of the technique. We give some data examples, which are compared with theoretical data in order to improve the interpretation of the data. We then turn to the properties of all recorded eruptions (702 in all) before finishing with a discussion of our results in comparison with earlier studies.

2 DESCRIPTION OF THE EXPERIMENT

From 2000 April 27 until May 7 we recorded eruption velocities during strombolian eruptions on Stromboli volcano, Italy, using a

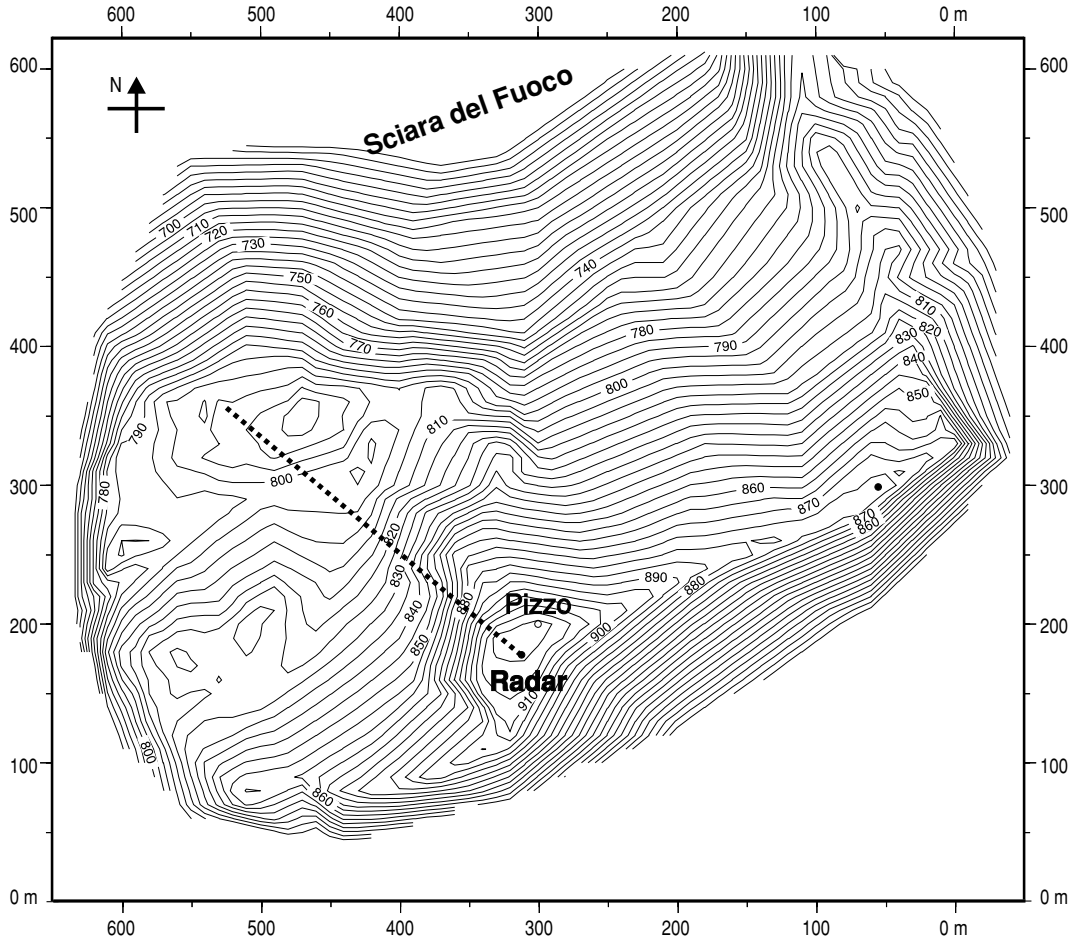

Figure 1. Topographic map of the top region of Stromboli. Data are based on a survey made in 2000 September and are taken from Urbanski *et al.* (2002). The topographic situation in 2000 September was basically the same as during 2000 May. The Doppler radar was set up near the Pizzo Sopra la Fossa as indicated by the solid circle and the direction of the radar beam is shown by the straight line. The instrument was tilted 23.1° downwards towards crater 1b and is approximately 300 m away from the active vent.

Doppler radar. Our FM–CW Doppler radar was installed on the top of Stromboli volcano near the Pizzo Sopra La Fossa (see Fig. 1). This location is on the rim of the crater terrace at the upper end of the Sciara del Fuoco, a collapse scar that was formed during the last collapse event at Stromboli volcano about 5000 yr ago (Rossi *et al.* 2000; Tibaldi 2001). The instrument was set up approximately 280 m away from the near rim of one of the active vents (crater 1b, see Fig. 1) and the radar beam had an inclination of 23.1°. The distance to the far end of vent 1b is about 350 m. These distances were measured using a vector GIS (by Leica) and the readings are precise to about ±10 m (the uncertainty is much higher than that given by the manufacturer (±0.3 m (15–500 m) ±1 m up to 1000 m) and is due to the large amount of hot gases in the vicinity of the vents that make reading the instrument much more difficult than under normal conditions).

The most important change in observational conditions occurred on April 29, when a severe rain storm including thunder and lightning passed over the island. Unfortunately, the batteries of the instrument were mostly empty on April 28 due to a broken charge controller. We planned to replace everything on April 29, but the rain storm (which lasted for several hours) made service of the instrument impossible. We were thus unable to restore the instrument back into operation until the afternoon of April 30.

2.1 Description of the measurement principle

A Doppler radar detects the frequency shift occurring between the transmitted and backscattered electromagnetic wave. This frequency shift, ω, is directly proportional to the velocity of an object moving along the beam. One of the key features of the instrument is a mixing diode typically used in motion detectors or for velocity measurements by the police. This mixing diode is used for receiving the backscattered electromagnetic wave while simultaneously mixing it with part of the transmitted wave. The phase difference ϕ between the transmitted and received signal, ϕ, generates a phase-dependent voltage $U \propto \sin(\phi)$ (homodyne principle), which is measured precisely. Following Peters (1995) the phase shift is

$$\phi = \phi_t - \phi_r = 2rk, \tag{1}$$

where r is the distance to the target and $k = 2\pi/\lambda_t$ is the radar wavenumber. The subscripts t and r refer to the transmitted and the received signal, respectively.

The phase ϕ becomes time dependent if an object is moving along the beam at a given speed $v = r/t$, where t represents time. In this case the phase difference

$$\phi = \omega_d t \tag{2}$$

where

$$\omega_d = 2vk \tag{3}$$

is the Doppler shift due to the velocity v. Measuring ω_d, however, does not give any information regarding the distance of the object from the source. This can be determined by modulating the transmitted wave with, for example, a saw tooth function, such that

$$k = k_0 + tK/T. \tag{4}$$

Here K is the wavenumber of the modulation bandwidth, T is the modulation period and k_0 is the wavenumber of the carrier frequency. Please note that the radar wavenumber k is from now no longer constant and $1/T$ is also called the sweep frequency f_s. Using the frequency-modulated wavenumber (4) and inserting it into eq. (1) allows ϕ to be calculated from

$$\phi = 2rtK/T + \phi_0 = \omega_r t + \phi_0, \tag{5}$$

where ϕ_0 is a constant phase shift depending only on the transmitted frequency. The frequency ω_r depends on the distance of the object from the source,

$$\omega_r = 2rK/T. \tag{6}$$

In order to determine the velocity and the distance of a moving target, ω_d and ω_r have to be measured simultaneously. This problem has been solved by Strauch (1976). Briefly, if one compares two consecutive modulation periods, one finds that due to the changing distance of a moving target, a phase shift difference $\Delta\phi$ occurs,

$$\Delta\phi = 2rK = 2vTk_0 \tag{7}$$

between two consecutive cycles. Thus, for a resting target $\Delta\phi = 0$. A spectral analysis of a large number of consecutive modulation periods for resting or even no targets results in a frequency spectrum with lines at multiples of $1/T$ (see Fig. 2a). Strauch (1976) was able to show that the power of the nth line of such a spectrum comes out of a scattering volume of depth ΔR, where

$$\Delta R = \pi/K = c/(2f_m) \tag{8}$$

at a distance of $n\Delta R$. Here $n \in \mathcal{N}$, $n = \text{round}(f/f_m)$ (Klugmann *et al.* 1996), c is the speed of light and f_m is the maximum modulation frequency, respectively. Varying the maximum modulation frequency, f_m, changes the scattering volume depth ΔR (see eq. 8). The depth intervals ΔR are also termed range gates.

In a perfect system a target resting at, for example, $2\Delta R + 0.3\Delta R$, would only leave a signal at the frequency $2/T$. As a result of the non-perfect depth discrimination between neighbouring lines, however, a resting object located between $n\Delta R$ and $(n + 1)\Delta R$ will result in nearly equal signals at lines n/T and $(n + 1)/T$ (see Fig. 2a, lines $2/T$ and $3/T$ for the example given above with a resting target at $2\Delta R + 0.3\Delta R$). In addition, one will also find a weak imprint of that object in the neighbouring lines $(n - 1)/T$ and $(n + 2)/T$ (see Fig. 2a lines $1/T$ and $4/T$ for the example given above with a resting target at $2\Delta R + 0.3\Delta R$).

For a target moving through the beam at distance $n\Delta R$ the phase difference between two consecutive cycles is no longer zero (see eq. 7). Furthermore, due to the change in distance between two consecutive modulation periods, the phase difference is also no longer periodic with the modulation period, T. In this case Strauch (1976) was able to show that the line n/T, representing a resting target at distance $n\Delta R$, is shifted by the Doppler frequency ω_d, if the target moves at speed v in the direction of the beam (see Fig. 2b). Obviously a problem will occur, once $\omega_d > 2\pi f_s = 2\pi/T$. Therefore, the maximum velocity, v_{max}, that can be resolved unambiguously in each range gate can be derived using eq. (3) and the relationship $\lambda = c/f$

$$|v|_{max} = \frac{c}{2}\frac{f_0}{f_s}. \tag{9}$$

A similar manipulation leads to the general relationship between the frequency shift Δf and velocity v (e.g. Klugmann *et al.* 1996)

$$v = \frac{c}{2}\frac{\Delta f}{f_0} \pm \left(\frac{c}{2}\frac{\delta f}{f_0}\right), \tag{10}$$

in which $\Delta f = f - nf_s$ is the frequency shift due the velocity of a target at a distance $n\Delta R \pm \Delta R/2$. Parameter δf is the minimum

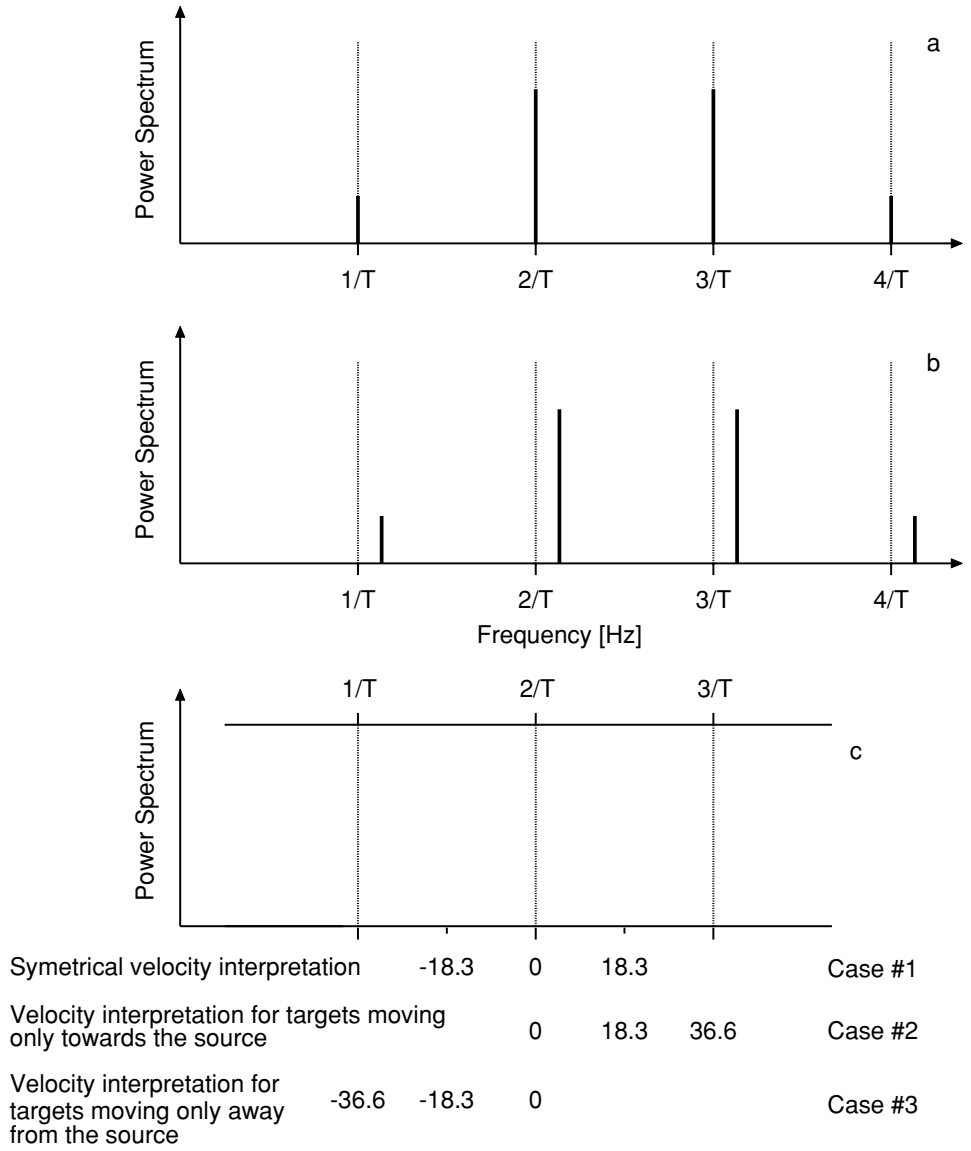

Figure 2. Power spectra for a target at $2.5\Delta R$ once resting (a) and once moving towards the source (b). At the frequencies $1/T$, $2/T$, etc. the velocity for the respective range gates is equal to zero. Part (c) shows the various possibilities to interpret the velocities measured for a range gate at distance $2\Delta R$.

frequency resolution that converts straight into a minimum velocity resolution $\delta v_{\min}$,

$$\delta v_{\min} = \frac{c}{2}\frac{\delta f}{f_s}. \tag{11}$$

For more details on this the reader is referred to a much more comprehensive and detailed description by Strauch (1976), Chadwick & Strauch (1979) or Peters (1995).

2.2 Description of the instrument

At Stromboli we used a significantly modified commercially available microradar (MRR-3). This instrument is normally used as a rain gauge for meteorological measurements (Klugmann *et al.* 1996). The instrument is a compact FM–CW Doppler radar with a nominal transmission power of 50 mW at a frequency of 24 GHz. After being amplified, windowed, comb notch and low-pass filtered, the received signal is digitized at 187.5 kHz so that a bandwidth of up to 93.75 kHz can be resolved. The sweep frequency $f_s = 1/T$ is equal to 5.859, 375 Hz, i.e. 16 range gates are resolved. The maximum modulation bandwidth f_m of 5 MHz gives a range gate depth ΔR of 30 m.

The resulting power spectrum (backscattered energy as a function of frequency), in which the backscattered power of all targets along the beam are superimposed contains 2048 points, i.e. $\delta f = 45.78$ Hz. The minimum velocity resolution (see eq. 11) is 0.2859 m s^{-1}, and the maximum velocity along the beam that can be unambiguously resolved in each range (see eq. 9) is 36.6 m s^{-1}. Using the general relationship between frequency and velocity, eq. (10), the power spectrum can be converted into a velocity power spectrum, i.e. the backscattered energy as a function of distance and velocity.

As explained above, the frequencies n/T mark the zero velocity for targets at a distance of $n\Delta R \pm \Delta R/2$. There are now several ways to interpret frequencies in the range $(n-1)/T < f < (n+1)/T$ in terms of velocities, three of which are shown in Fig. 2(c) cases 1–3. Case 1: all spectra are interpreted such that it is assumed that all particles move towards the instrument, i.e. only frequencies in the range $n/T \leq f < (n+1)/T$ will occur and velocities therefore

range from 0 to 36.6 m s^{-1} in each range gate. Case 2: all particle are moving away from the instrument, such that the frequency range of interest is $(n-1)/T < f \leq n/T$ and velocities therefore range from -36.6 to 0 m s^{-1} in each range gate. Case 3: the *a priori* direction of targets is not known so that the best assumption is a symmetrical interpretation in which $n/T - 1/(2T) < f < n/T + 1/(2T)$. In this case the velocities now vary between -18.3 and 18.3 m s^{-1}. However, any other distribution around n/T is possible. In our case we almost always use the symmetrical interpretation (case 3) because the direction of the targets is not known. The other interpretations (cases 1 and 2) are used when, for example, rainfall is observed while the instrument is pointing vertically upward. With a symmetrical interpretation, velocities along the beam larger or smaller than 18.3 m s^{-1} are wrapped into the neighbouring range gates (this occurs when $\omega_d/2\pi$ becomes larger than $1/2T$, see the discussion above and Section 2.3). A careful visual data analysis and manual data processing, however, also allows an interpretation of those more complex velocity power spectra.

The antenna of the system is a 60 cm diameter offset parabola. The radar beam has an aperture of approximately 2°. Careful measurements of the intensity distribution inside the beam by the manufacturer of the instrument showed that with an opening of 0.75° the two-way damping is equal to 6 dB and the intensity distribution is best fitted by a Gaussian curve using $\sigma = 0.5$. The instrument continuously transmits and receives a signal and incoming data are stacked and averaged until they are interrogated by the data logger. The interrogation intervals can be as low as 1 s. In this case 10–11 stacked spectra are averaged, with each spectrum including 128 sweeps.

2.3 Data example

Fig. 3 shows two 4 s long recordings from the evenings of April 27 (Fig. 3a) and April 30 (Fig. 3b). Each recording shows the onset of an eruption, the first record shows the last second prior to the onset of the eruption and the next three are the first three seconds of the eruption. The recordings for each second (from top to bottom) show the reflectivity in six range gates (each 30 m long) extending from 240 to 390 m. Inside each range gate the left-hand part of each spectrum represents particle that move away from the instrument and the right-hand part particle that move toward the instrument. As explained earlier velocities along the beam that are higher than 18.3 m s^{-1} will be mapped into neighbouring range gates. An example for this is given in Fig. 3(b) (second record), where the maximum speed of particle along the beam towards and away from the instrument is at least about 30 m s^{-1}. This interpretation is based on the fact that the highest amplitude has been recorded in the 330 m range gate. Because velocities higher than 18.3 m s^{-1} are mapped into neighbouring range gates the velocity range can be extended for such a signal (this extension is indicated by the velocities printed in *i* below the second recording shown in Fig. 3b). We have to admit, however, that estimating velocities larger than those which map into the appropriate range gate is not as precise as determining velocities below 18.3 m s^{-1}, because they are overprinted on the original signal for that specific range gate.

As a result of signal processing details inside the radar instrument, particle that are recorded in one range gate also leave a small imprint in neighbouring range gates (see also above). This is especially visible in Fig. 3(a) within the second, third and fourth recordings: in these cases the signals recorded in range gates 2 (270 m) and 5 (360 m) are in this case regarded as 'mirror images' and are thus not considered in any further data processing. The signals in range gates 3 (300 m) and 4 (330 m), however, show the beginning of an eruption. The decision, as to which range gate contains a true signal is more or les straightforward, because we know that the eruption is rather localized and therefore the strongest signals are always the true signals.

So far all the velocities reported have been in the direction of the radar beam. Different eruption vectors **V**, however, can result in the same velocity v_b recorded by the radar (see Fig. 4). In order to better understand these recorded signals we first model different eruption scenarios and determine the theoretically recorded signal.

3 THEORETICAL CONSIDERATIONS

The model developed for calculating theoretical radar spectra has two parts: the first describes the eruption itself and the second calculates the energy reflected by the eruption and recorded by the radar. There are generally two ways of modelling an eruption, either by solving the equations for momentum, mass and energy conservation (e.g. Woods 1988; Dobran 2001), or by simply prescribing a velocity distribution, an opening angle, an eruption inclination and a particle size. Because we are interested in the relationship between eruption parameters and the radar signal we prescribe, like others (Ripepe *et al.* 1993), all eruption values rather than using a general eruption dynamics model. The applicability of such a model to strombolian eruptions remains somewhat unclear due to the special dynamics of strombolian eruptions (e.g. Seyfried & Freundt 2000).

We assume that during strombolian eruptions particle travel ballistically, which is easily verified by examining video recordings of strombolian eruptions as well as long-term exposure photos of eruptions. The particle trajectories of material ejected out of the vent can be calculated assuming Stokian friction between particle and air from

$$m\ddot{\mathbf{r}} = -\beta\dot{\mathbf{r}} - mg\mathbf{e}_3, \tag{12}$$

where **r** is the distance to the position along the trajectory, m is the mass of the particle, g is the acceleration due to gravity, $\mathbf{e}_3$ is the unit vector in the z-direction and β is the friction coefficient. With the following initial conditions:

$$\begin{aligned}\mathbf{r}(t=0) &= x_0\mathbf{e}_1 + y_0\mathbf{e}_2 + z_0\mathbf{e}_3,\\ \mathbf{V}(t=0) = \mathbf{V}_0 &= V_{xy_0}\cos\alpha_0\mathbf{e}_1\\ &\quad + V_{xy_0}\sin_0\alpha\mathbf{e}_2 + V_0\sin\gamma_0\mathbf{e}_3,\ V_{xy_0} = V_0\cos\gamma_0.\end{aligned} \tag{13}$$

Eq. (12) can be solved analytically for V_x, V_y, V_z and **r** as a function of time. In eq. (13) x, y and z are the directional components of **r** and α, γ are the angle between V_{xy} and the x-axis and **V** and V_{xy} (see Fig. 5). The subscript 0 denotes the initial conditions.

A projection of the velocity vector $\mathbf{V} = (V_x, V_y, V_z)$ of an individual particle at **r** on to a line in the direction of **r** (i.e. a line connecting the origin of the global coordinate system and the current location of the particle) gives the velocity v_l of that individual particle along that specific line

$$\begin{aligned}v_{lx}(t) &= \cos\alpha_x V_x(t), \quad v_{ly}(t) = \cos\alpha_y V_y(t),\\ v_{lz}(t) &= \cos\alpha_z V_z(t), \quad v_l(t) = -[v_{lx}(t) + v_{ly}(t) + v_{lz}(t)].\end{aligned} \tag{14}$$

Here $\alpha_{x,y,z}$ are the angle between the x, y, z axes of the coordinate system and the connecting line, respectively.

With the velocity v_l along a line connecting source and particle being known, we can calculate the reflected signal that will be recorded by the radar system located in the centre of the global coordinate system. The reflected power P_r is calculated from (Probert-Jones 1962)

$$P_r = \frac{C}{r^2}|\mathcal{K}|^2 Z, \tag{15}$$

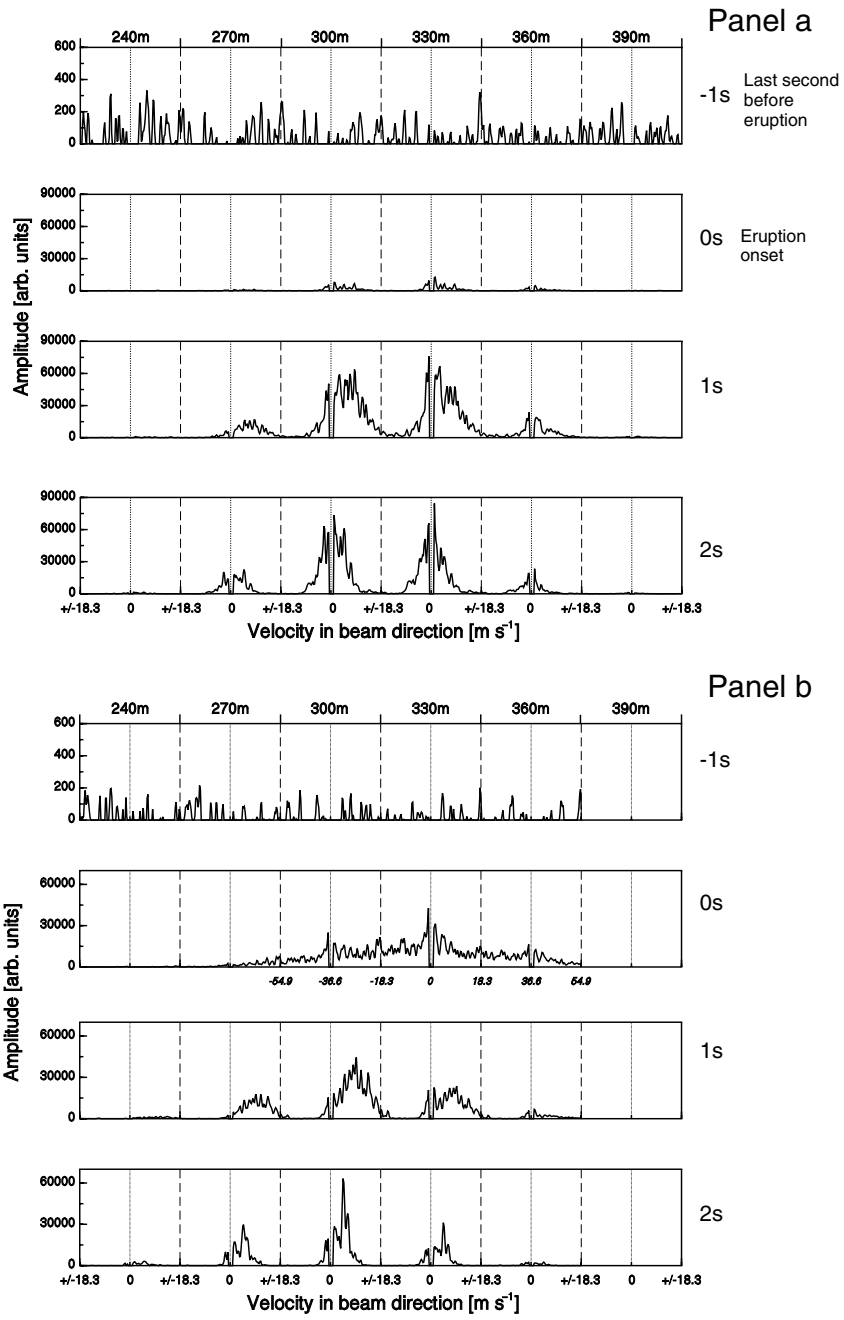

Figure 3. Two 4 s recordings of the onset of eruptions 2000 April 27 at 20:49:03 (a) and 2000 April 30 at 20:24:08 (b). Please note the different scale in the *y*-axis between the first and the other three recordings in each part of the figure. Each record shows the velocity distribution recorded in different range gates. The distance to the centre of each range gate from the radar instrument is given on the top *x*-axis (see Fig. 1 for the location). For each range gate negative velocities represent particle moving away from the instrument and positive velocities particle that move towards the instrument. The velocity is the velocity in the beam direction. For details of the interpretation see the text.

where C is an instrument constant that has to be measured separately and $\mathcal{K}$ is the complex refractive index

$$\mathcal{K} = \frac{\epsilon - 1}{\epsilon + 2}, \tag{16}$$

with ϵ being the dielectrical constant. $\mathcal{K}$ has been measured for volcanic ash for frequencies up to 19 GHz by Adams *et al.* (1996) and has a value of 0.39 ± 0.02. Z is the radar reflectivity (in units of $\mathrm{mm}^6\ \mathrm{m}^{-3}$) which, assuming Rayleigh scattering, can be calculated from

$$Z = \sum D_\mathrm{p}^6 = \int_0^\infty N(D_\mathrm{p}) D_\mathrm{p}^6\, dD_\mathrm{p}, \tag{17}$$

where $N(D_\mathrm{p})$ is the number density of particle (number/(m^3 m)) of size D_p. From eq. (17) it is clear that a few large particle generate the same reflectivity as a large number of small ones.

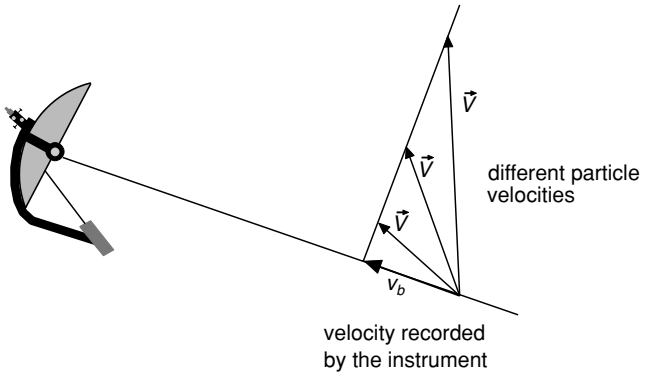

Figure 4. Illustration of the relationship between the true particle velocity and the recorded particle velocity.

The particle position with respect to the beam centre changes as a function of time (see eq. 12) and the intensity of the radar beam is a function of the distance from the beam centre (see above, Section 2.2 and Fig. 5). Therefore, the reflected energy is: (1) a function of the distance from the beam centre and (2) a function of the absolute distance r from the source, eq. (15). By calculating the angle between the radar beam fixed in space and the vector **r** connecting the radar source (here the origin of the global coordinate system) and the current location of the particle of interest, we can determine the intensity of the beam at that location. Given this intensity the determination of the intensity of the signal backscattered by a single particle is straightforward using eq. (15).

For calculating the theoretical velocity power spectra, we track the trajectories of 20 000 spherical particle of uniform size. The particle size was chosen to be 1 cm as this is fairly representative for the typical particle size at Stromboli (Kokelaar & Romagnoli 1995). Their density is fixed at 1200 kg m^{-3}, resulting in a mass of 5 g for each particle. Particle of such a density contain about 50 vol. per cent vesicals, which is a common content of vesiculated scoria at Stromboli volcano (Kokelaar & Romagnoli 1995). In order to solve eq. (12) we have to prescribe the initial conditions. The centre of the eruption is fixed at x_0, y_0 and z_0. Next we either need to prescribe V_x, V_y and V_z or prescribe V_0 and the angle α and γ (see Fig. 5). We chose to prescribe V_0, which varies randomly between a prescribed lower and an upper limit. The initial direction of the individual particle that belong to the eruption is determined by two angles, α_0 and γ_0, which are prescribed in such a way that they all fall into an inverted cone of prescribed opening, the tip of which coincides with the eruption centre. The centre line of the cone is the initial eruption

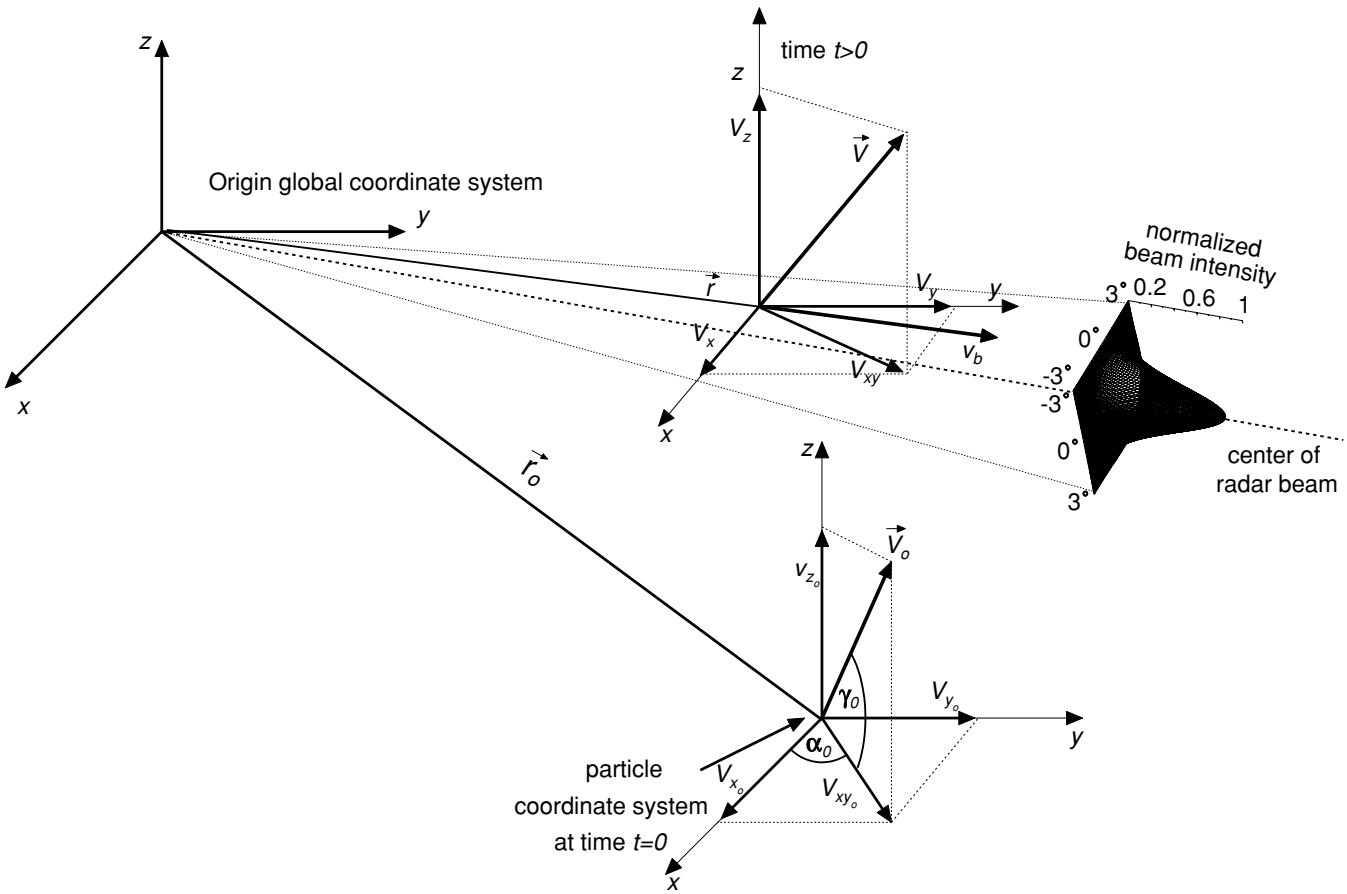

Figure 5. Illustration of the different coordinate systems used in the model calculations simulating the reception of the Doppler radar. In addition to the radar beam (thick dotted line), the aperture and the approximate power distribution of the beam are shown. For the meaning of the various velocity vectors and velocity components see the text.

Table 1. Parameter used in the standard model as well as their variation range while exploring their impact on the radar spectra.

Value	Unit	Standard value	Variation range
Eruption inclination γ	deg	90	30–90
Opening angle of the eruption	deg	90	30–120
Lower velocity	m s^{-1}	0	0–50
Upper velocity	m s^{-1}	50	20–100
Depth of eruption (z-direction)	m	−150	−120 to −170
Horizontal position of eruption (x-direction)	m	285	260–300
Horizontal position of eruption (y-direction)	m	0	0–200

inclination and γ_0 is the prescribed initial inclination of individual particle trajectories. The resulting inclination frequency distribution for the individually erupted particle is assumed to be Gaussian and centred around the centre line of the inverted cone. The angle in the (x, y) plane, α_0 (see Fig. 5) varies randomly between 0° and 360°. In all calculations it is assumed that all particle are erupted at time $t = 0$.

3.1 Synthetic radar data

The different values for calculating synthetic spectra are listed in Table 1 along with their variation range. The beam inclination (centre of the radar beam) was chosen to be equal to the inclination of the beam during our experiment at Stromboli in 2000 April/May (−23.1°). During the model calculations all values were fixed at their standard value, while one parameter was varied systematically. The spectra calculated for the first 5 s for our standard model eruption (see Table 1) are shown in Fig. 6 along with the distribution of initial particle trajectory inclinations (γ_0 in Fig. 5). A comparison of Figs 3(a) and 6 shows that the general features of the velocity power spectra are the same, except that in our model particle only leave a signal imprint in one range gate, i.e. we do not account for the effect of 'mirror images' discussed above (see the lines with lower amplitudes at $1/T$ and $4/T$ in Fig. 2b). The simulated data should therefore only be compared with data in that range gate where we recorded the highest reflectivities, because this is the range gate where the particle physically pass the beam.

Comparing the amplitudes of the received signals at different times for the recorded and simulated spectra (Figs 3 and 6), the signal observed during the first second of the eruption is weak compared with the signal during the remainder of the eruption. This is fairly easy to understand as in the case of the simulated velocity power spectra, the eruption centre is assumed to be 30 m below the centre of the beam. Therefore, only the fastest particle are seen by the beam during the first second of the eruption. This leads to a shift of the velocity power spectrum to higher velocities early on. During the first second of the eruption, the maximum velocity in direction of the beam is at about 7.5 m s^{-1}. Converting it into a vertical velocity we find nearly 19.2 m s^{-1}, which is much lower than the highest initial eruptive velocity at the assumed vent, which is equal to 50 m s^{-1}. However, this is not surprising as the ejecta lose some of their kinetic energy during the first 30 m of travel due to increase in height and friction. In fact, this velocity of 19.2 m s^{-1} is exactly equal to the velocity a particle ejected vertically at 50 m s^{-1} will have while passing through the beam centre 30 m above the vent. Later during the eruption the slower particle are detected by the beam, shifting the peak in the velocity power spectrum to smaller values (compare the first and second recordings in Fig. 6).

The velocity distribution for falling particle is much narrower than the one for rising particle. This is mainly due to the fact that we consider only one particle size and therefore the particle reach their terminal settling velocities. Interestingly, a conversion of the peak settling velocity into a particle size gives about 1 cm, which is the value we used in the model calculation. In addition, in all simulations the velocity distribution for settling particle is always narrow, regardles of the initial conditions. This means that if the recorded velocity power spectra show a narrow velocity distribution for settling particle the grain size distribution of the erupted material is narrow too. Therefore, a conversion of the settling velocities into a particle size is valid, even though it is based on the assumption that the particle settle vertically. This is not the case, for example, if strong winds blow the particle in one direction.

While varying the different parameter (see Table 1), we found that the eruption inclination, the depth of the eruption below the beam centre and the maximum initial ejection velocity have the biggest impact on the simulated spectra (see Fig. 7). Increasing the maximum velocity from 50 m s^{-1} in the standard model (Fig. 6) to 70 and 100 m s^{-1} (Fig. 7a) significantly broadens the velocity peak during the first 2 s of the eruption. In these two examples it is particularly obvious how high velocities map into neighbouring range gates (see the high-velocity tail of the eruption during the first second, which maps into the 300 m range gate). In the case of very strong eruptions it is therefore impossible to simply divide the signals into each range gate. However, the continuous signal that extends over more than one range gate, i.e. velocity mapping, is easy to detect and therefore it can be accounted for during the data processing (see Fig. 3 and above).

Reducing the eruption inclination from 90° to 60° and 30° results in a shift of the velocity distribution observed in the spectra. For an inclination of 90° (i.e. a vertical eruption) the initial velocity distribution (Fig. 6) exhibits only positive velocities save for a very small tail of the distribution in the negative velocity field. Decreasing the eruption inclination to 60° (Fig. 7b) we find the initial velocity distribution to be centred, i.e. the maximum reflectivity occurs at 0 m s^{-1}. Because in all calculations the beam inclination is 23.1° downwards the angle between the eruption and the beam is nearly 90° in this case (60° eruption inclination), giving rise to a nearly centred velocity distribution. For an inclination of 30° (Fig. 7b) the velocity distribution moved completely into the field of negative velocities. In addition, for this eruption inclination the signal becomes very weak (compare with the amplitudes of the different calculations) because only a small number of particle passes through the radar beam due to the low eruption angle. Furthermore, due to the low eruption angle the particle trajectories cut through the radar beam such that the velocity component of individual particle seen by the radar beam becomes negative.

Moving the eruption source closer to the beam centre by 15 m compared with the standard model (there the source was 30 m below the beam centre) and in a second calculation into the beam centre significantly changes the recorded signal (Fig. 7c). The

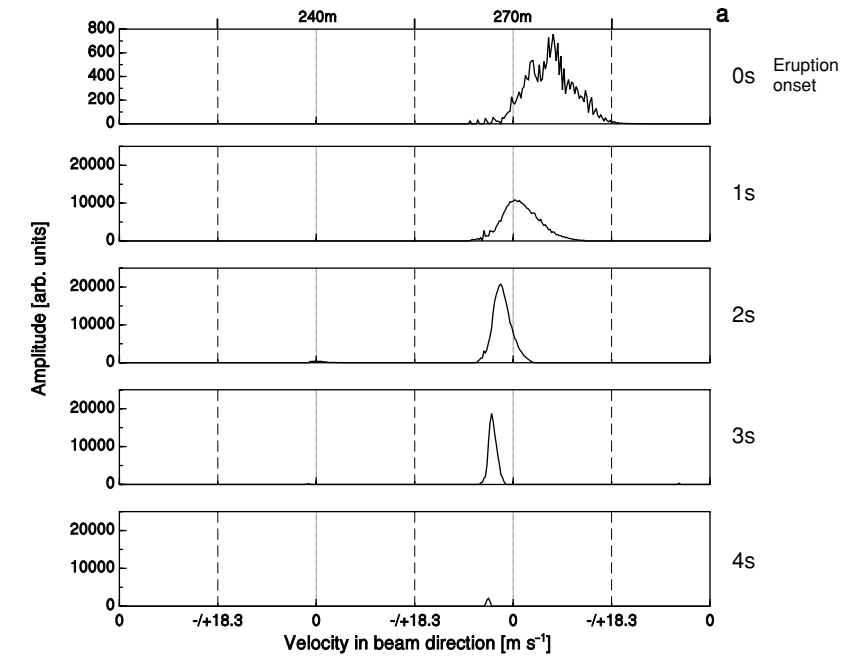

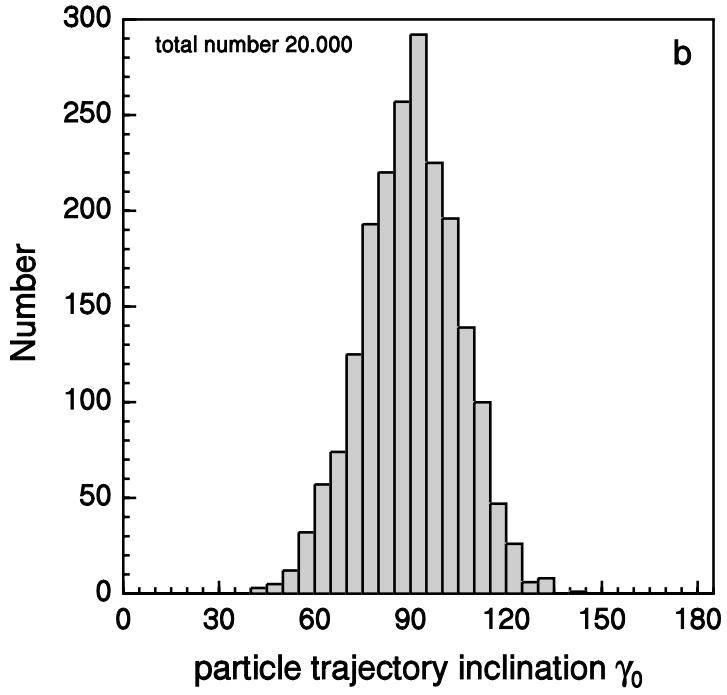

Figure 6. The first 5 s of a simulated eruption (a) using the standard values listed in Table 1. Most of the eruption signal is only recorded in the 30 m range gate centred around 285 m because the eruption centre is located at $x_0 = 285$ m, $y_0 = 0$ m and 30 m below the beam centre and we do not account for 'mirror images'. Please note the different scale of the y-axis for the first and the following seconds. Part (b) shows a histogram of the distribution of the particle trajectory inclinations centred around the eruption inclination of 90°. The opening angle in this calculation was 90°.

spectra become smoother and the reflections stronger compared with the standard model. This behaviour is easy to understand. In the standard model the eruption is 30 m below the beam centre. As a result of the opening angle of the eruptive fountain of about 30° (see Fig. 6b) the diameter of the eruption column is about 40 m when passing through the beam centre. When the eruption centre moves closer to the beam centre this diameter decreases and in the case of the beam centre coinciding with the eruption source it is a point source. Therefore, the closer the source is to the beam centre the more particle are recorded by the beam, leading to an increase in reflected power and to smoother spectra.

Moving the eruption centre 15 m into the y-direction leaves only the imprint of falling particle in the calculated spectra. The rising particle are no longer seen because they do not pass through the beam in this case. Moving the eruption in the direction of the x-axis

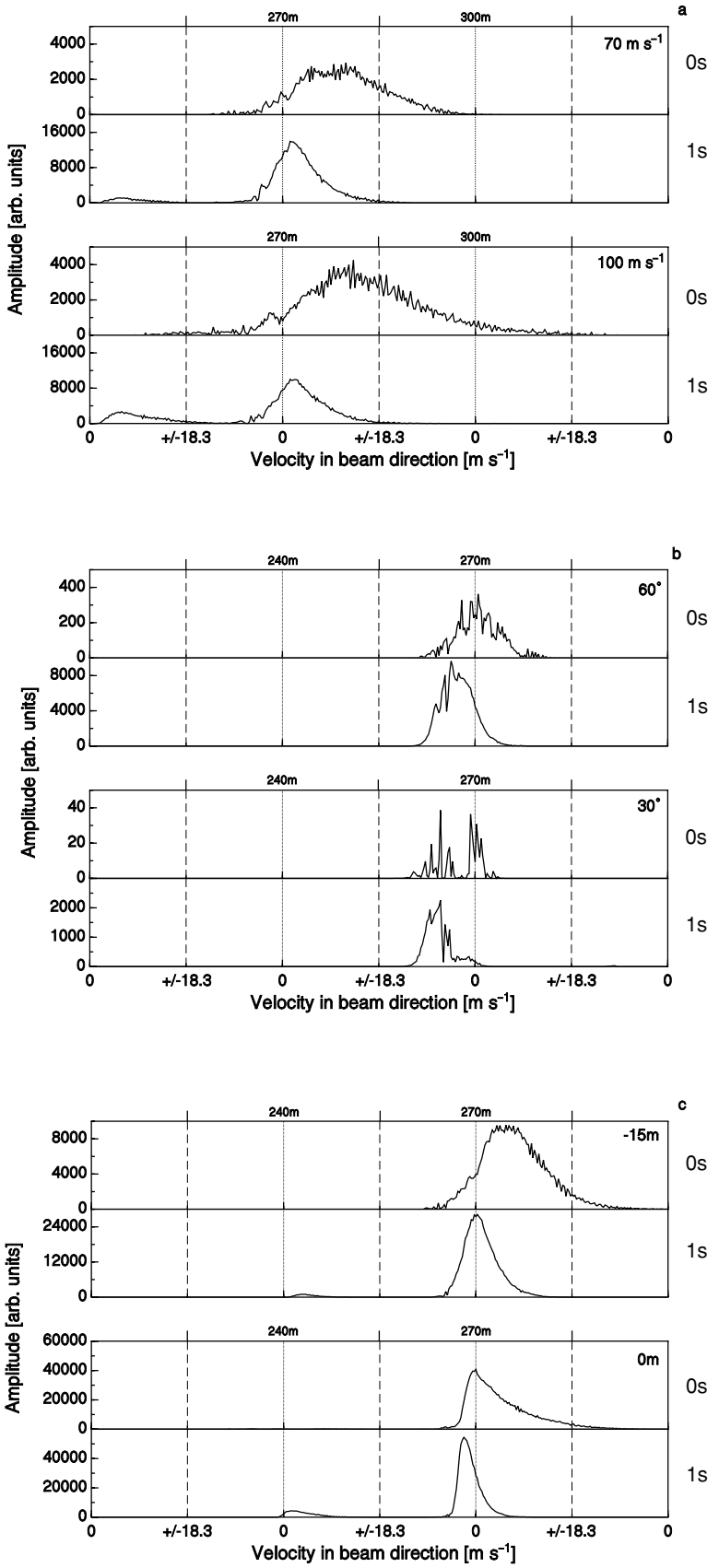

Figure 7. The first 2 s of six different simulated eruptions. Panel (a) shows two calculations where the upper eruption velocity bound has been increased. The impact of varying the eruption inclination is shown in (b) and (c) shows the variation of source of the eruption. The parameters used in these calculations are listed in Table 1. For details on the interpretation of the different signals see the text. Please note the different scale of the *y*-axis in each panel.

moves the signal from one range gate to another with nearly similar signals being recorded if the eruption centre is located at 275 m in the x-direction. The general shape of the velocity distribution, however, does not change compared with the standard model except that the amplitude decreases with increasing distance, eq. (15). Increasing the speed of the slowest particle erupted from 0 to 50 m s^{-1} shifts the peak of the velocity distribution a bit to higher velocities, but the shape of the distribution remains once again more or less untouched.

From the different example discussed above it is obvious that the recording of the first second of an eruption is the most important, because one captures almost only particle moving upward. The signal recorded during the 1 s of the eruption is very sensitive to the actual angle of the eruption, allowing a zeroth-order estimate of the eruption inclination as well as the maximum velocity.

4 DATA PROCESSING

As demonstrated above, a certain type of velocity distribution can be generated by a couple of different parameter sets, which makes a straightforward inversion of the recorded 1-D data for the true eruption velocity impossible. In order to characterize the eruptions recorded by the instrument in some way we have thus established a set of coefficients that characterize the eruption. For the velocity spectrum recorded in each range gate we define

$$P_{\mathrm{R}}^{+}(t) = \sum_{0}^{v_{\max}} P_{\mathrm{r}}(v, t) \tag{18}$$

and

$$V^{+}(t) = \frac{1}{P_{\mathrm{R}}^{+}(t)} \sum_{0}^{v_{\max}} P_{\mathrm{r}}(v, t) v. \tag{19}$$

Here $P_{\mathrm{r}}(v, t)$ is the recorded reflected power as a function of the velocity v and time t and the superscript '+' refers to particle with positive velocities. Because the reflected power $P_{\mathrm{r}}(v, t)$ is related to the actual amount of material moving at speed v, the product of $P_{\mathrm{r}}(v, t)v$ can be interpreted as the momentum and $V^{+}(t)$ is the mean momentum velocity for rising particle. For particle with positive velocities the summation boundaries range from 0 to $v_{\max}$, where $v_{\max}$ is the maximum velocity that can be resolved in each range gate, i.e. 18.3 m s^{-1} in the case of a symmetrical velocity interpretation (see the discussion of Fig. 2c, case 3). For the initial seconds of very strong eruptions, however, $v_{\max}$ has to be increased in order to capture the whole velocity distribution (see the discussion on mapping of high velocities above).

In the case of particle with negative velocities the sums in eqs (18) and (19) run, of course, from $-v_{\max}$ to 0. Obviously, for very strong eruptions $-v_{\max}$ has to be decreased in some cases. $P_{\mathrm{R}}^{-}(t)$ and $P_{\mathrm{R}}^{+}(t)$ are the energy reflected by all scatterers that moved through the radar beam during one measurement. A direct conversion of $P_{\mathrm{R}}^{-}(t)$ and $P_{\mathrm{R}}^{+}(t)$ into a mass is impossible, because the reflected power is not a linear function of the particle size (see eq. 15) and the relation between particle speeds and particle size is unknown. There is, however, good evidence in the data (almost constant $V^{-}(t)$ values between eruptions) that the particle size distribution does not change significantly as long as the eruption style remains the same (see below). In this case a relative change in $P_{\mathrm{R}}^{-}(t)$ and $P_{\mathrm{R}}^{+}(t)$ does represent relative changes in ejected mass.

During the discussion of the simulated spectra we saw that the power velocity distribution for falling particle is rather narrow. If the particle settle with their terminal settling velocities, their speed is indicative of their size, provided they settle vertically, i.e. there is no wind influence. We can therefore define an average particle size D_{p}, which can be calculated from the speed of the falling particle. Based on the terminal settling velocities of rain drops (Rogers & Yau 1989) we define

$$D_{\mathrm{p}}(t) = \frac{\mathcal{C}}{P_{\mathrm{R}}^{-}(t)} \sum_{-v_{\max}}^{0} P_{\mathrm{r}}(v, t) v^{2}, \tag{20}$$

where $\mathcal{C}$ is a shape factor, which is equal to $3/4 c_{\mathrm{d}} \rho_l / (\rho_b g)$, with c_{d} being the drag coefficient, g being the gravitational acceleration and ρ_l, ρ_b being the density of air and ejected material, respectively. Eq. (20) shows that $D_{\mathrm{p}}(t)$ is weighed with the reflectivity $P_{\mathrm{r}}(v, t)$.

Because the coefficients ($P_{\mathrm{R}}^{+}(t)$, $V^{+}(t)$, etc.) are calculated for each recorded spectrum one can obviously sum the coefficients obtained for each spectrum to obtain

$$\overline{P_{\mathrm{r}}^{+}} = \sum_{t_{\mathrm{e}}} P_{\mathrm{R}}^{+}(t) \tag{21}$$

over the length of an entire eruption t_{e}. Here $\overline{P_{\mathrm{R}}^{+}}$ is the total reflected energy of each eruption for either particle with negative $\overline{P_{\mathrm{R}}^{-}}$ or positive $\overline{P_{\mathrm{R}}^{+}}$ velocities and provides a crude estimate for the total amount of material that moved through the beam with positive or negative velocities during the entire eruption. The average momentum eruption velocity $\overline{V^{+}}$ can be calculated in a similar manner by summing

$$\overline{V^{+}} = \frac{1}{\overline{P_{\mathrm{R}}^{+}}} \sum_{t_{\mathrm{e}}} V^{+}(t) P_{\mathrm{R}}^{+}(t) \tag{22}$$

over the entire duration of the eruption. Again this sum can be calculated for particle with positive and negative velocities. Finally, we can also determine the average size $\overline{D_{\mathrm{p}}}$ in a similar fashion.

The recorded data are automatically scanned for eruptions by first subtracting the background noise from each spectrum. The noise spectrum is the temporal average of the three spectra before the case being processed. Eruption onsets are detected by setting a threshold value for $P_{\mathrm{R}}^{+}(t)$. The length of the rise phase of an eruptive event is the time from onset until $P_{\mathrm{R}}^{+}(t)$ drops again below a fixed threshold. While processing an eruption the noise is removed from the data using the last calculated noise spectrum before the eruption onset. We manually checked a large number of eruptions for accuracy of eruption onset identification and found our procedure to be very precise. The end of an eruption, and therefore also its length, is once again determined by a threshold, meaning $P_{\mathrm{R}}^{-}(t)$ drops below a prescribed value. The choice of this threshold may change the length of the eruption by 1–2 s, so our estimated eruption length is not as precise as our eruption onset. However, we used the same threshold values for the entire data set and therefore the calculated values are at least internally consistent.

As shown in Fig. 4 the radar records only the velocity component of particle along the radar beam. As a result of the setup of our instrument at Stromboli volcano (see the beginning of Section 2), reporting a velocity in the direction of the 23.1° inclined beam is not very useful because visual observation indicates that the erupted material moves more or less vertically. We have demonstrated above (see the simulated spectra) that at least for eruptions that are nearly vertical the speeds calculated by projecting the velocity along the beam on to a vertical direction correctly recovers the vertical component of the particle while moving through the beam. The assumption of a nearly vertical eruption, however, remains to be proven. We have shown through our theoretical modelling that once the inclination of the eruption changes significantly from the vertical, the

velocity power spectra recorded at the onset of an eruption are significantly shifted towards negative or positive velocities. Taking our setup in the field and our experience from the simulations, the onset of a nearly vertical eruption has a small contribution in the negative velocity field and most of the signal is recorded in the positive velocity field (see Fig. 7a). Because nearly all of our recorded data show these characteristics, we are confident in our conversion of the velocities recorded along the beam during our experiment into vertical velocities.

5 CHANGES IN ERUPTIVE STYLE

Fig. 8 shows the various coefficients defined above as a function of time for the two eruptions shown in Fig. 3. For the eruption

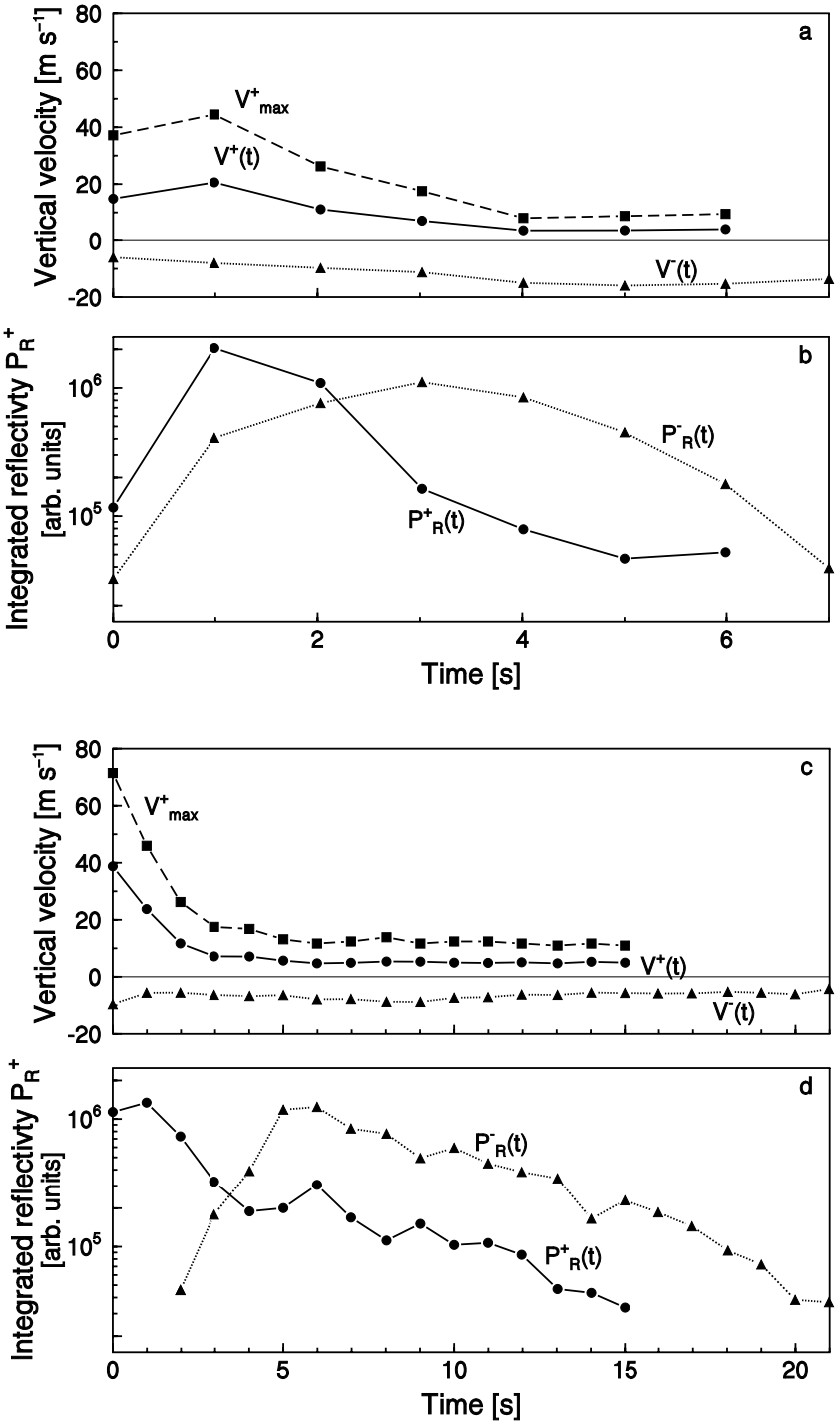

Figure 8. Temporal evolution of the mean vertical momentum velocities $V(t)$ for rising (solid line in a, c) and settling particle (dotted lines in a, c) as well as maximum vertical velocities for rising particle (dashed lines in a, c) for the two eruptions shown in Figs 3(a) and (b). Panels (b) and (d) show the integrated reflectivities for rising (solid lines) and settling particle (dotted lines) as a function of time.

on April 27, we find the average momentum speed, $V^+(t)$, of the ejected particle first increases up to about 19 m s^{-1} (see Fig. 8a, solid line) and then decreases (all velocities reported from now on are vertical velocities, see above). The change in momentum velocity is mirrored by an increase and then a decrease in reflectivity for ejected particle, $P_R^+(t)$ (Fig. 8b, solid line). Initially the maximum velocity of the rising particle (Fig. 8a, dashed line) is close to 44 m s^{-1} and then it drops too. The momentum velocity of the falling particle $V^-(t)$ increases slightly during the eruption from about 8 m s^{-1} to about 14 m s^{-1} (see Fig. 8a, dotted line). The maximum reflectivity for falling particle is observed 2 s after the maximum reflectivity of the rising particle occurred.

From the temporal evolution of the different coefficients we can also calculate an average momentum velocity for the entire eruption, $\overline{V^+}$, which in this case is about 16 m s^{-1} for the rising particle and about 12 m s^{-1} ($\overline{V^-}$) for settling ones. If the settling particle descend with their terminal settling velocities, one can convert the average settling speed into an average grain size, which is in this case about 8 mm.

The temporal evolution of the coefficients for the eruption on 2000 April 30 is shown in Figs 8(c) and (d). Comparing the two eruptions the first obvious difference is that the April 30 eruption lasts much longer than that on April 27. In addition, the maximum velocity (dotted lines) and momentum velocity (solid lines) of the rising particle $V^+(t)$ are significantly larger, suggesting a much more violent eruption on April 30 (compare the solid lines in Figs 8a and c): the initial maximum particle speed is close to 70 m s^{-1} compared with 44 m s^{-1} for the other example (compare dotted lines). Interestingly, however, the settling momentum velocities $V^-(t)$ of the particle (Fig. 8c, dashed line) on April 30 are significantly smaller and the reflectivity maximum for settling particle $P_R^-(t)$ occurs significantly later (5 s later than the reflectivity maximum for the rising particle).

From the temporal evolution of the different coefficients we can again calculate average momentum velocities for the entire eruption, which in this case is about 19 m s^{-1} for the rising particle ($\overline{V^+}$) and about 8 m s^{-1} for settling ones ($\overline{V^-}$). The average grain size D_p is about 3 mm, which is a factor of 2–3 smaller than the average size during the April 27 eruption. From Figs 8(a) and (c) it is also obvious how the thresholding works. If the reflectivity of either $P_R^+(t)$ or $P_R^-(t)$ rises above 1500 units an eruption start is detected and if it drops below 1500 units it is assumed that the eruption ends. We should note that during non-eruptive periods $P_R^+(t)$ and $P_R^-(t)$ are of the order of 100 for the remaining background noise. The end of the rise phase is determined if $P_R^+(t)$ becomes less than 2 per cent of the maximum reflectivity detected during an eruption.

After discussing the differences between two single events, we turn to the properties of all eruptions recorded between 2000 April 27 and May 6. A total of 702 eruptions were observed. From those 132 occurred before a major rain storm. The remaining 570 occurred after the storm. Because we had already found a significant difference in the length of the two case type eruptions before and after the rain storm, we first examined the length of the rise phase and total eruption length as a function of time (see Fig. 9). Clearly, the length of the rise phase (Fig. 9a) as well as the eruption length (Fig. 9b) change significantly from before to after the rain storm. This is also evident from histograms of the rise phase length (Fig. 9c) as well as the eruption duration (Fig. 9d). The histograms before and after the rain storm are significantly different. However, the ratio of rise time to total eruption length remains nearly constant, it drops from about 0.8 before the rain storm to about 0.7 after the rain storm.

The main reason for the significantly longer eruption duration after the rain storm is mainly the longer phase of descending particle. The rise phase length does increase on average from 6 to 10 s, whereas the total eruption length increases on average from 8 to 15 s (Fig. 9). In general one can change the total eruption duration by either reducing the gas overpressure (i.e. driving material more slowly out of the conduit) or increasing the gas volume involved in the eruption. A pure reduction of the gas overpressure will lead to lower eruption velocities, which is not observed here; we find them to increase after the rain storm. Therefore, we feel that the gas volume driving the eruption must have increased. If, in addition, the gas overpressure changed at the same time is something we cannot answer from our data.

Through the analysis of our settling velocities we have shown that the average particle size does decrease from before to after the rain storm (see Fig. 10c). Furthermore, we find longer periods of particle descend that can be caused either by increasing the energy of eruptions throwing material to much greater height (in this case the particle size does not necessarily need to change) and/or by making fragmentation much more efficient, thereby reducing the particle size and therefore the terminal settling velocities (see Figs 10a and b). In the case of our data it is probably a combination of both, as we generally see increased eruption velocities after the rain storm but also reduced settling speeds and therefore smaller grain sizes (see Fig. 10c). Both of these scenarios are also consistent with the possible increase in gas volume discussed above.

In order to make sure that the differences found (see Fig. 9) are not a cumulative effect of the 570 events after the rain storm but occur directly after the rain storm we also processed only a small subset (the first 132 eruptions) of the eruptions after the rain storm and compared that distribution with the distribution found for all 570 events after the rain storm. The distributions are found to be nearly identical, suggesting that the pattern of eruptions did not change during the 570 events recorded after the rain storm.

Although the eruption length increased significantly after the rain storm, the intervals between the eruptions remained nearly constant (see Fig. 11) from before to after the rain storm. The only slight difference is found at an eruption interval of 700 s where an additional peak in the distribution before the rain storm (light grey bars in Fig. 11) occurs, which is not found after the rain storm. However, considering the small number of events before the storm compared with those after the storm this is considered to be not significant.

With the eruption intervals not changing and the length of the eruptions increasing (see above), we expect changes in the amount of erupted material. Although we cannot calculate the absolute amount of erupted material from our data, the coefficient $\overline{P_R^+}$ (see eq. 21) is at least a qualitative measure of the total erupted mass. While interpreting $\overline{P_R^+}$, however, one has to bear in mind that two eruptions with exactly the same erupted mass but different grain size distributions do not result in the same reflectivity due to the strong dependence of the reflected energy on the grain size (see eq. 15). For example, one spherical clast 1 cm in diameter is erupted in one eruption and in another eruption the same mass is erupted by two clasts of 0.79 cm in diameter. In this case the reflectivity of the two clasts is half that of the reflectivity of the single clast in the case of Rayleigh scattering and 0.62 in the case of geometrical optics. In the case of Mie scattering (Mie 1908, in the case of Mie scattering the particle diameter is on the order of the wavelength and the intensity of the scattered energy becomes a strong function of the material as well as surface properties) we expect the ratio to be between 0.5 and 0.62. In addition the reflectivity may be influenced by the surface

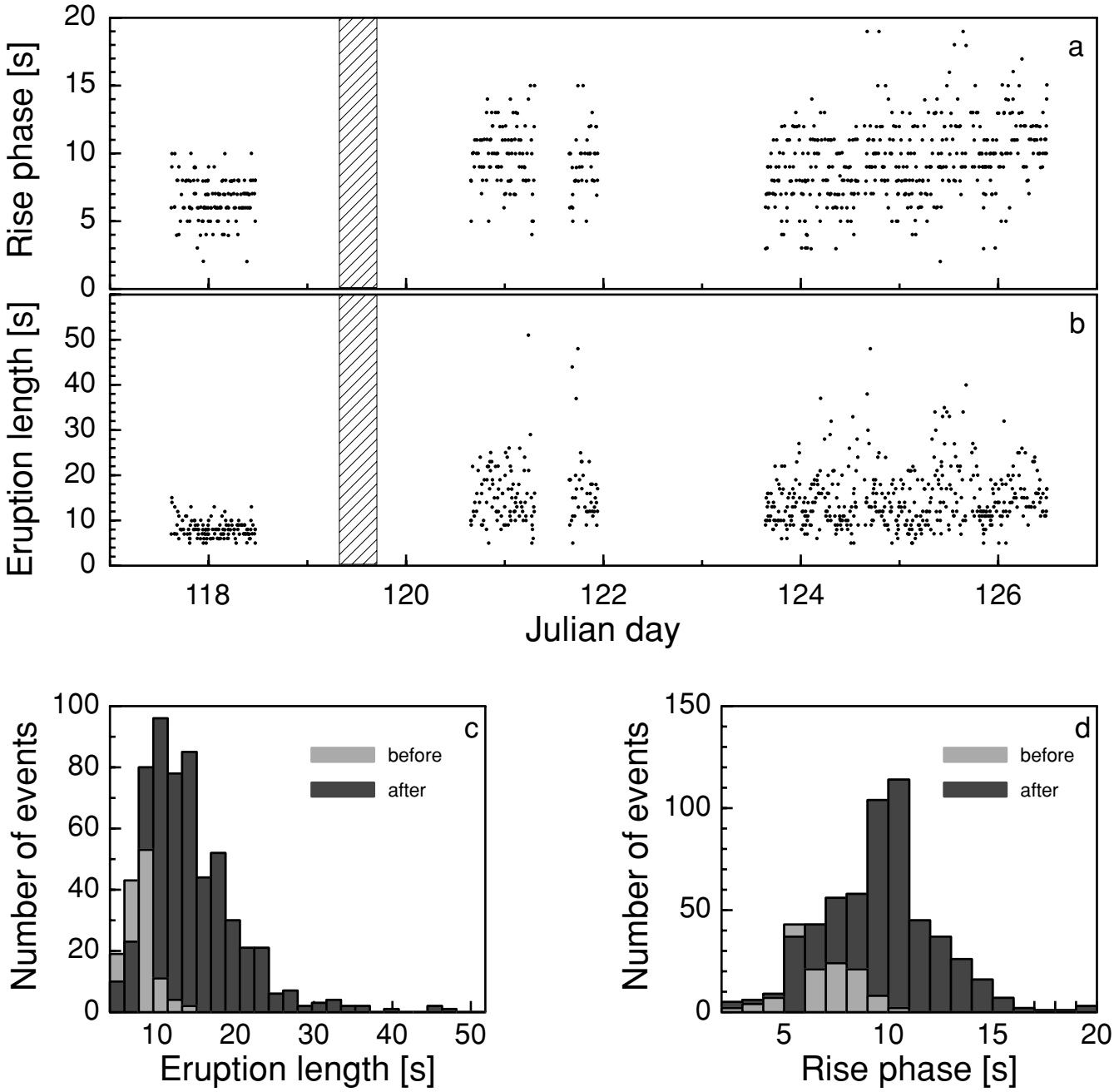

Figure 9. Variation of the rise phase length (a), as well as the total eruption length (b) as a function of time. The horizontal alignment of the data points is due to the fact that our temporal resolution is 1 s. The shaded area in the upper two panels indicates the approximate duration of the rain storm. Panels (c) and (d) show histograms of the rise phase length (c) as well as the eruption length (d) before (light grey) and after (black) the rain storm. The mean rise phase length before and after the rain storm are 6 ± 2 s and 10 ± 3 s, respectively. The mean eruption length changes from 8 ± 2 to 15 ± 7 s.

properties of the clasts, which will, however, not vary much from one eruption to the next. Keeping this in mind, we find the reflectivity of the eruptions after the storm to be larger than before it (see Fig. 12, please note that on the x-axis we have plotted $\log(\overline{P_R^+})$). Because we have shown above that the average particle size is smaller after the rain storm, it is safe to interpret the increase in reflectivity as an increase in the amount of erupted material. With the eruption intervals remaining constant the amount of material transported through crater 1b after the rain storm definitely increased.

6 DISCUSSION AND CONCLUSIONS

In this study we explored the eruption dynamics of one of the vents of Stromboli volcano, Italy, using a newly designed Doppler radar system. The idea behind our study is in many ways comparable to the work of Ripepe *et al.* (1993), however, we recorded many more events, although we did not record the seismic activity associated with the different explosions simultaneously. We were able to show that the eruption dynamics changed during our observational period from very short-lived explosive events to longer-lasting explosions.

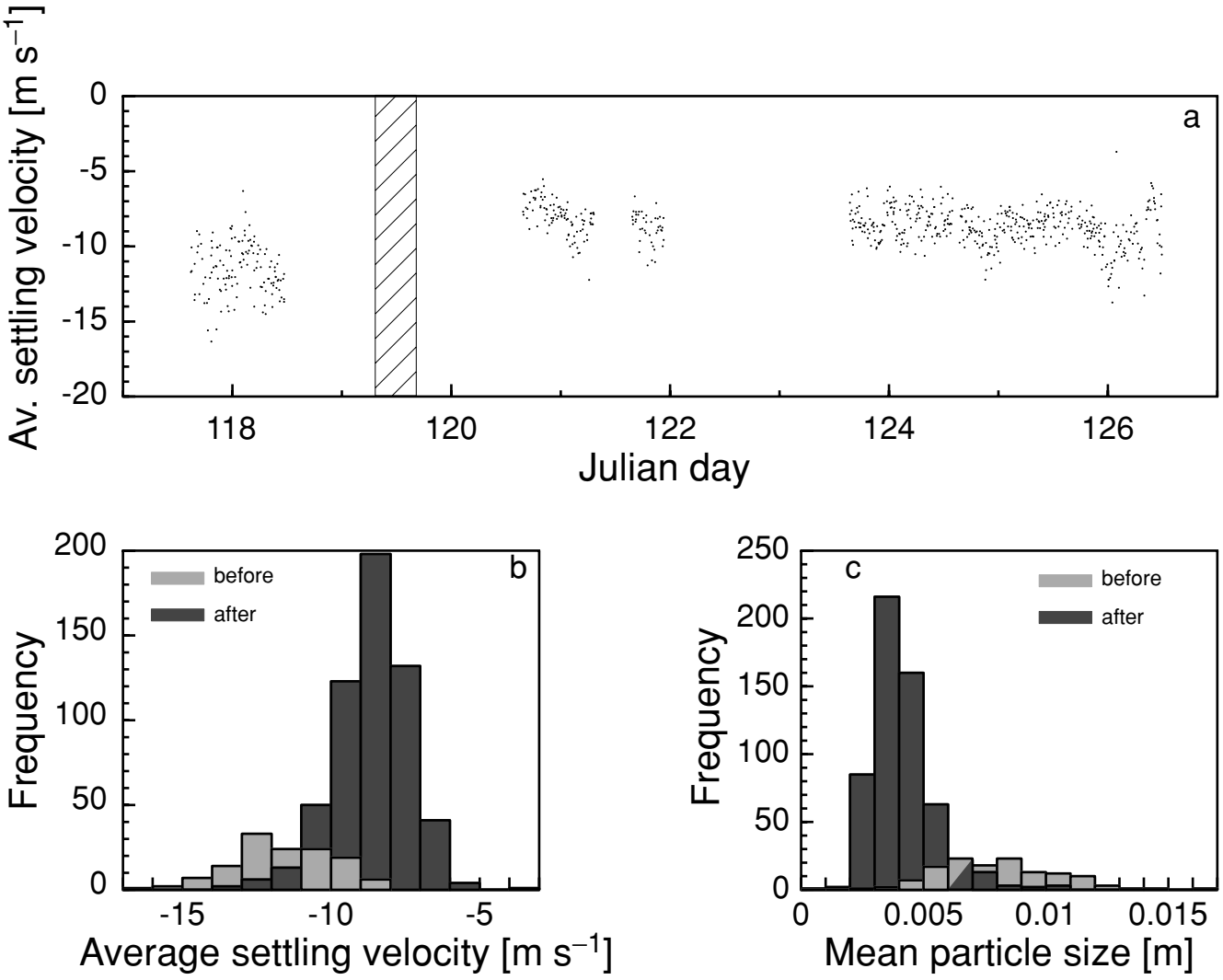

Figure 10. Variation of the settling velocity as a function of time (a) and a comparison of the average settling velocities (b) as well as average settling particle sizes before (light grey) and after (black) the rain storm. The mean particle settling size before and after the rain storm are 8 ± 2 mm and 4 ± 1 mm, respectively. The shaded area in the upper panel indicates the approximate duration of the rain storm.

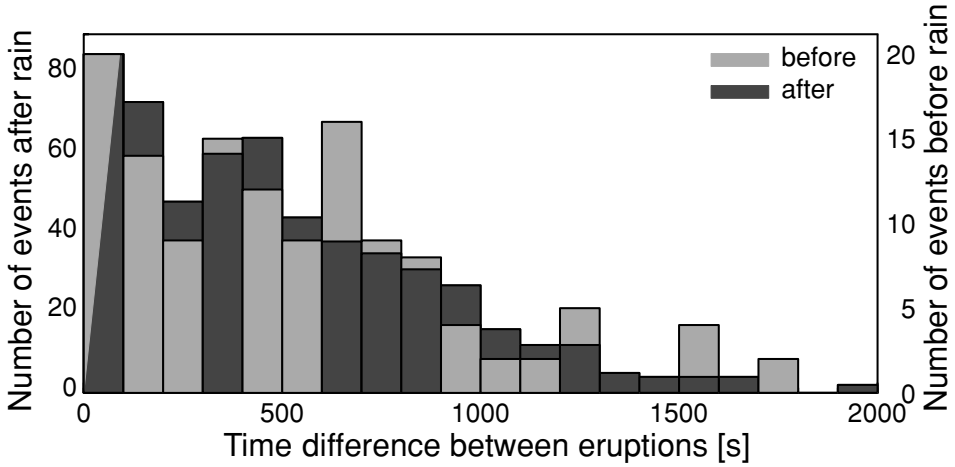

Figure 11. Time differences between eruptions before (light grey) and after (dark grey) the rain storm.

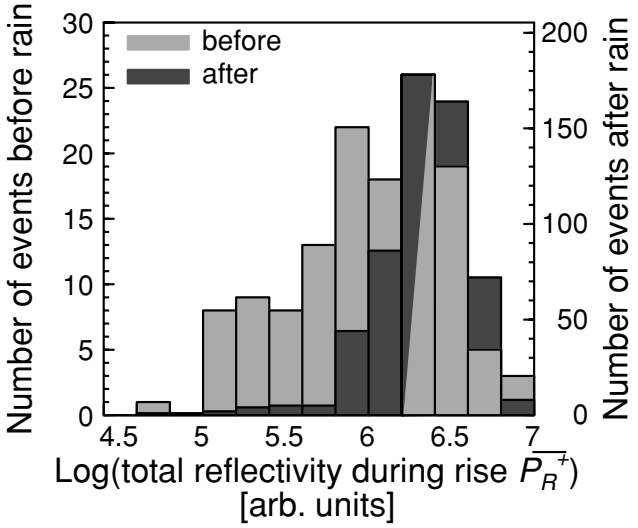

Figure 12. Total reflectivity during the rise phase of the eruptions before (light grey) and after (dark grey) the rain storm. The means are 6.0 ± 0.46 and 6.30 ± 0.34, respectively. Please not that on the *x*-axis the logarithm of the total reflectivities has been plotted.

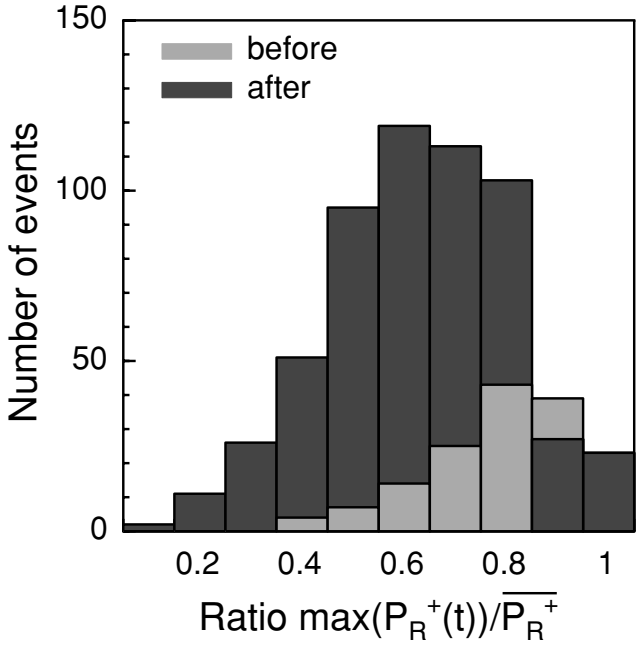

Figure 13. Ratio of the maximum reflectivity $P_R^+(t)$ recorded during an eruption and $\overline{P_R^+}$. If this ratio is close to 1 all material is ejected during a very short time. If it tends towards 0.1 or less material ejection occurs over a longer period of time. Ratios close to 1 can be associated with explosive eruptions (burst of one large bubble), ratios of 0.5 or less show signs of fountaining eruptions that are driven by the ascent of several bubble.

The occurrence of short-lived explosions is a well-known characteristic of Stromboli volcano (e.g. Chouet *et al.* 1999; Neuberg 2000), but has so far mostly been characterized by seismological and acoustic methods (e.g. Ripepe & Gordeev 1999).

The eruption velocities determined by our method are in the range of velocities that have been determined in former studies of the activity at Stromboli volcano (Chouet *et al.* 1974; Blackburn *et al.* 1976; Weill *et al.* 1992; Ripepe *et al.* 1993; Hort & Seyfried 1998). Only the studies by Weill *et al.* (1992) and Ripepe *et al.* (1993) discuss the temporal evolution of different eruptions in detail. Ripepe *et al.* (1993) were able to identify three different types of eruptions, where in types one and two the material is ejected in one single pulse or two pulses following each other with only very little time in between. The third type is characterized by a slow increase in the eruption rate. In our case most of the eruptions were characterized by a single explosive event, where the maximum speeds and strongest reflectivities occur during the first 2 s of an eruption (see also Fig. 13). Generally this behaviour is associated with the bursting of single bubble. Our observations of eruption behaviour are comparable to the observations made by Ripepe *et al.* (1993) at the southwest crater in 1989. However, the same crater did produce quite different eruption signatures in 1988 with an increasing mass flux culminating after 3–5 s (Ripepe *et al.* 1993). This behaviour is explained by the explosion of several bubble generating a fountain-like behaviour. The interesting part of this observation is, however, that the same crater exhibits quite different eruptive patterns.

Chouet *et al.* (1974) did not report the temporal evolution of the ejected material but the variation of the mean eruption velocity as well as single and bulk velocity distributions. In their study Chouet *et al.* (1974) picked two eruptions, which they considered to be end-member cases. Eruption 1 is a rather strong explosive event with a slowly decaying eruption velocity. The rise phase of this eruption lasted for 8 s. The other eruption (eruption 2) is a weak event where the rise phase lasted 4 s. Both times have been estimated from Fig. 7 in Chouet *et al.* (1974). The velocity distributions for both eruptions are very similar to those found during our study and the temporal evolution of eruptions for the weak explosion (eruption 2 in their paper) is very similar to those observed by us before the rain storm. Eruptions like their eruption 1, however, were not observed very often, indicating the dominance of single explosive events (see also Fig. 13).

Both studies discussed show that changes in eruptive behaviour are common at Stromboli, but the mechanisms for changes in eruptive behaviour are, however, still unclear. One interesting aspect of our experiment is the well-documented change in explosive activity at the observed vent. There is a coincidence of the change in volcanic activity and a rain storm that passed over the island. The impact of rainfall on volcanic activity is conceivable but its documentation through hard data is rather scarse. For example, a study at Arenal Volcano, Costa Rica, did not reveal any significant correlation between seasonal rainfall and the intensity of pyroclastic flows (Vidal & Melson 1999). In our case, however, we feel that we have possible evidence for such an interaction, but we hasten to admit that this is a single observation and therefore it may be completely fortuitous. In the following we will first discuss our evidence for magma–rainwater interaction and then briefly review other possibilities for changing the eruptive style.

In the case of our study the details of the rainwater–magma interaction remain unclear and there is at least one possible model for this interaction that we feel is reasonable: after the rain storm water constantly infiltrates the magmatic system, thereby increasing the amount of volatile driving explosions and fragmentation, or, after the rain storm the interaction of the rain water with the magma led to some larger explosions that reshaped the vent, giving rise to a change in eruption dynamics. In both cases, however, the rain must have migrated towards the magma. Whereas the case of reshaping the vent is very hard to prove, there should be a strong meteoric signature in the volcanic gases in the case of a constant infiltration of water. This has indeed been observed at Stromboli volcano. Gas analysis of fumarolic gases at Stromboli volcano indicates a strong influence

of meteoric water in the gas plume (Martini 1991). Metrich & Allard (2002) found that the H_2O flux in the volcanic plume is an order of magnitude higher than would be expected from melt inclusions, also strongly supporting the impact of meteoric water. Both observations therefore suggest a constant influx of meteoric water into the volcanic system supporting the first of our models. How exactly the water enters into the magmatic system, however, remains unclear but a recent study by Finizola *et al.* (2002) documents the existence of several hydrothermal cells in the upper edifice of Stromboli volcano. Those hydrothermal systems could provide pathways for rain water into the conduit system leading to the proposed interaction.

Besides our observation changes in eruptive style have been found on various timescale in several earlier studies and in contrast to our situation were observed during stable weather conditions (see above and Ripepe *et al.* 2001, 2003). In those cases the variation in eruptive activity is explained through other models, which may also apply in our case considering that we have only one observation of such a possible rainwater–magma interaction. Based on extensive seismic, acoustic and thermal measurements Ripepe *et al.* (2003) suggest that variations in the eruptive style are due to changes of the influx of magmatic volatile combined with a variation in the magma level in the conduit (see also Ripepe *et al.* 2001). Switching from one style to another occurs over a matter of minutes, suggesting a fast process is responsible for the switching. Blackburn *et al.* (1976) tie higher gas jet velocities to higher gas pressures or higher gas bubble concentrations, thereby allowing one to explain the variations exclusively through degassing and not through variations in the magma level in the conduit. Which of these models would actually apply to our observation is unclear, however the occurrence of the change in eruptive style after the rain storm is somewhat striking and we have given some indications as to why such rainwater–magma interactions appear to be a plausible explanation for our observation.

ACKNOWLEDGMENTS

We would like to thank N. Urbanski for his tremendous help in the field and M. Ripepe and A. Harris for extended discussions on strombolian activity. Reviews by A. Harris and M. Ripepe significantly improved the manuscript. This research was supported by the Deutsche Forschungsgemeinschaft through grant Ho1411 10-1.

REFERENCES

Adams, R.J., Perger, W.F., Rose, W.I. & Kostinski, A., 1996. Measurements of the complex dielectric constant of volcanic ash from 4 to 19 GHz, *J. geophys. Res.,* **101,** 8175–8185.

Aster, R., Lees, J. & Neuberg, J., 2000. Broadband seismic and acoustic observations of volcanic seismicity (editorial), *J. Volc. Geotherm. Res.,* **101,** vii–viii.

Blackburn, E.A., Wilson, L. & Sparks, R.S.J., 1976. Mechanism and dynamics of strombolian activity, *J. geol. Soc. Lond.,* **132,** 429–440.

Chadwick, R.B. & Strauch, R.G., 1979. Processing of FM–CW Doppler signals from distributed targets, *IEEE Trans. Aerosp. Electron. Syst.,* **ASE15,** 185–189.

Chouet, B., Hamisevicz, N. & McGetchin, T.R., 1974. Photoballistics of volcanic jet activity at Stromboli, Italy, *J. geophys. Res.,* **79,** 4961–4976.

Chouet, B.S.G., Dawson, P., Martini, M., Scarpa, R., De Luca, G., Milana, G. & Cattaneo, M., 1999. Broadband measurements of the source of explosions at Stromboli volcano, Italy, *Geophys. Res. Lett.,* **26,** 1937–1940.

Dehn, J., Harris, A.J.L. & Ripepe, M., 2001. Infrared imaging of strombolian eruptions, *EOS, Trans. Am. geophys. Un.,* **82,** F1411.

Dobran, F., 2001. *Volcanic Processes: Mechanisms in Material Transport,* Kluwer/Plenum, New York.

Dubosclard, G., Cordesses, R., Allard, P., Hervier, C., Coltelli, M. & Kornprobst, J.S.O., 1999. First testing of a volcano Doppler radar (Voldorad) at Mount Etna, Italy, *Geophys. Res. Lett.,* **26,** 3389–3392.

Finizola, A., Sortino, F., Lenat, J.-F. & Valenza, M., 2002. Fluid circulation at Stromboli volcano (Aeolian Island, Italy) from self-potential and CO_2 surveys, *J. Volc. Geotherm. Res.,* **116,** 1–18.

Head, J.W. & Wilson, L., 1987. Lava fountain heights at Pu'uO'o, Kilauea Hawaii: indicators of amount and variations of exsolved magma volatile, *J. geophys. Res.,* **92,** 13 715–13 719.

Herzog, M., Graf, H.-F., Textor, C. & Oberhuber, J.M., 1998. The effect of phase changes of water on the development of volcanic plumes, *J. Volc. Geotherm. Res.,* **87,** 55–74.

Hort, M. & Seyfried, R., 1998. Volcanic eruption velocities measured with a micro radar, *Geophys. Res. Lett.,* **25,** 113–116.

Hort, M., Seyfried, R. & Vöge, M., 2001. Monitoring volcanic eruption velocities in three dimensions: first results from Doppler radar measurements at Stromboli volcano, *EOS, Trans. Am. geophys. Un.,* **82,** F1400.

Jaupart, C. & Vergniolle, S., 1988. Laboratory models of Hawaiian and strombolian eruptions, *Nature,* **331,** 58–60.

Klugmann, D., Heinsohn, K. & Kirtzel, H.-J., 1996. A low cost 24 GHz FM–CW Doppler radar rain profiler, *Beitr. Phys. Atmosph.,* **69,** 247–253.

Kokelaar, P. & Romagnoli, C., 1995. Sector collapse, sedimentation and clast population evolution at an active island-arc volcano: Stromboli, Italy, *Bull. Volcanol.,* **57,** 240–262.

Mader, H.M., Brodsky, E.E., Howard, D. & Sturtevant, B., 1997. Laboratory simulations sustained volcanic eruptions, *Nature,* **388,** 462–464.

Martini, M., 1991. Stromboli, activity report, *Bull. Gobal Volc. Network,* **16,** 20–21.

Metrich, N. & Allard, P., 2002. Open-conduit magma degassing at basaltic volcanoes: constraints from crystal melt inclusions and volatile fluxes at Stromboli (Aeolian island, Italy), in preparation.

Mie, G., 1908. Beiträge zur Optik trüber Medien, speziell kolloidaler Metallösungen, *Ann. Phys., Lpz.,* **4,** 377–445.

Neuberg, J., 2000. External modulation of volcanic activity, *Geophys. J. Int.,* **142,** 232–240.

Papale, P., 1999. Strain induced magma fragmentation in explosive eruptions, *Nature,* **397,** 425–428.

Peters, G., 1995. *Entwicklung des Micro Rain Radars MRR-1,* METEK Meteorologische Messtechnik GmbH, Elmshorn.

Probert-Jones, J.R., 1962. The radar equation in meteorology, *PhD thesis,* Department of Meteorology, London.

Proussevitch, A.A. & Sahagian, D.L., 1998. Dynamics and energetics of bubble growth in magmas: analytical formulation and numerical modeling, *J. geophys. Res.,* **103,** 18 223–18 251.

Ripepe, M., 1996. Evidence for gas influence on volcanic seismic signals recorded at Stromboli, *J. Volc. Geotherm. Res.,* **70,** 221–233.

Ripepe, M. & Gordeev, E., 1999. Gas bubble dynamics model for shallow volcanic tremor at Stromboli, *J. geophys. Res.,* **104,** 10 639–10 654.

Ripepe, M., Rossi, M. & Saccorotti, G., 1993. Image processing of explosive activity at Stromboli, *J. Volc. Geotherm. Res.,* **54,** 335–351.

Ripepe, M., Ciliberto, S. & Schiava, M., 2001. Time constraints for modeling source dynamics of volcanic explosions at Stromboli volcano, *J. geophys. Res.,* **106,** 8713–8727.

Ripepe, M., Harris, A. & Carniel, R., 2003. Thermal, seismic and infrasonic evidence of variable degassing rates at Stromboli volcano, *J. Volc. Geotherm. Res.,* **118,** 285–297.

Rogers, R. & Yau, M., 1989. *A Short Course on Cloud Physics,* Pergamon, Oxford.

Rossi, M., Bertagnini, A. & Landi, P., 2000. Onset of the persistent activity at Stromboli volcano (Italy), *Bull. Volcanol.,* **62,** 294–300.

Seyfried, R. & Freundt, A., 2000. Analog experiments on conduit flow, eruption behaviour, and tremor of basaltic volcanic eruptions, *J. geophys. Res.,* **105,** 23 727–23 740.

Seyfried, R. & Hort, M., 1999. Continuous monitoring of volcanic eruption dynamics: a review of various techniques and new results from a frequency-modulated radar Doppler system, *Bull. Volcanol.,* **60,** 627–639.

Strauch, R.G., 1976. Theory and application of the FM-CW Doppler radar, *PhD thesis,* Faculty of the graduate school, Boulder.

Tibaldi, A., 2001. Multiple sector collapses at Stromboli volcano, Italy: how they work., *Bull. Volcanol.,* **63,** 112–125.

Urbanski, N., Vöge, M., Seyfried, R., Rüpke, L., Petersen, T., Hanebuth, T. & Hort, M., 2002. 15 days of continuous activity survey at Stromboli volcano/Italy in late September 2000: Doppler radar, seismicity, infrared, soil humidity, and mapping of the crater region, *Int. J. Earth Sci.,* **91,** 712–721.

Vergniolle, S. & Brandeis, G., 1994. Origin of sound generated by strombolian explosions, *Geophys. Res. Lett.,* **21,** 1959–1962.

Vidal, A. & Melson, W.G., 1999. Seasonal rain fall variations of pyroclastic activity; a case study of Arenal Volcano, 1993 to 1999, *Geol. Soc. Am. Abstr. with Prog.,* **31,** 478–479.

Weill, A., Brandeis, G., Vergniolle, S., Baudin, F., Bilbille, J., Fevre, J.-F., Piron, B. & Hill, X., 1992. Acoustic sounder measurements of the vertical velocity of volcanic jets at Stromboli volcano, *Geophys. Res. Lett.,* **19,** 2357–2360.

Wilson, L. & Head, J.W., 1981. Ascent and eruption of basaltic magma on the Earth and Moon, *J. geophys. Res.,* **86,** 2971–3001.

Woods, A.W., 1988. The fluid dynamics and thermodynamics of eruption columns, *Bull. Volcanol.,* **50,** 169–193.

Woods, A.W., 1995. The dynamics of explosive volcanic eruptions, *Rev. Geophys.,* **33,** 495–530.